Space Weather

RESEARCH ARTICLE
10.1029/2018SW002068

# Extreme-Value Geoelectric Amplitude and Polarization Across the Northeast United States

**Jeffrey J. Love[1], Greg M. Lucas[1], Paul A. Bedrosian[2], and Anna Kelbert[1]**

[1]Geomagnetism Program, Geologic Hazards Science Center, U.S. Geological Survey, Denver, CO, USA, [2]Geology, Geophysics, and Geochemistry Science Center, U.S. Geological Survey, Denver, CO, USA

**Key Points:**
- One hundred year geoelectric amplitudes across the Northeast range from 0.05 to 25.44 V/km
- Geoelectric fields tend to be most (least) polarized at locations with high (low) geoelectric hazard
- High-amplitude geoelectric fields tend to be polarized in a direction orthogonal to the strike of the Appalachian Mountains

**Supporting Information:**
- Supporting Information S1

**Correspondence to:**
J. J. Love,
jlove@usgs.gov

**Citation:**
Love, J. J., Lucas, G., Bedrosian, P. A., & Kelbert, A. (2019). Extreme-value geoelectric amplitude and polarization across the Northeast United States. *Space Weather*, *17*, 379–395. https://doi.org/10.1029/2018SW002068

Received 27 AUG 2018
Accepted 20 DEC 2018
Accepted article online 26 DEC 2018
Published online 1 MAR 2019



**Abstract** Maps are presented of extreme-value geoelectric field amplitude and horizontal polarization for the Northeast United States. These maps are derived from geoelectric time series calculated for sites across the Northeast by frequency-domain multiplication (time-domain convolution) of 172 magnetotelluric impedance tensors, acquired during a survey, with decades-long, 1-min resolution time series of geomagnetic variation, acquired at three magnetic observatories. The maps show that, during intense magnetic storms, high geoelectric amplitude hazards are realized across electrically resistive, igneous and metamorphic rock of the Appalachian Mountains and the New England Highlands, while low geoelectric hazards are realized across electrically conductive, sedimentary rock of the Appalachian Plateau and the Mid-Atlantic Coastal Plain. From statistical extrapolation, once-per-century (100-year) geoelectric amplitudes are highest at a site in Virginia at 25.44 V/km (followed by a site in Maine at 21.75 V/km and a site in Connecticut at 19.39 V/km); 100-year geoelectric amplitude exceeds 10 V/km at 12 sites across the northeast; geoelectric amplitude is lowest at a site in Virginia at 0.05 V/km. Average errors for these values are estimated to be about 38%, or much less than the more than 2 orders of magnitude range seen in geoelectric amplitudes from one survey site to another across the northeast. It is noteworthy that geoelectric fields tend to be most (least) polarized at locations with high (low) geoelectric hazard. Furthermore, geoelectric fields over the Appalachians tend to be polarized southeast-to-northwest, or generally in a direction orthogonal to the southwest-to-northeast geological strike. Results reported here inform utility companies in projects for evaluating and managing the response of power grid systems to the deleterious effects of geomagnetic disturbance.

## 1. Introduction

The northeast is one of the most densely populated regions of the United States—the cities of Boston, New York, Philadelphia, Baltimore, and Washington, DC, along with numerous other surrounding cities and towns, comprise a megalopolis of national and international importance (e.g., Florida et al., 2008; Gottman, 1961; Vicino et al., 2007). The northeast is supported by an intricate network of systems for the generation, transmission, and distribution of electric power (e.g., Abraham, 2002) that have, for various reasons, occasionally failed, resulting in widespread blackouts (e.g., Nye, 2010). Northeastern power grid systems have also experienced occasional operational stress during intense magnetic storms—that of 13–14 March 1989 caused numerous operational "anomalies" in northeastern power grid systems (North American Electric Reliability Corporation, NERC, 1990) and it damaged a high-voltage transformer at the nuclear power plant in Salem, New Jersey (Barnes et al., 1991; Rossi, 1990). The same storm precipitated the collapse of the Hydro-Québec power grid system to the north, in Canada (Béland & Small, 2005; Bolduc, 2002), leaving 6 million people without electricity for 9 hr (e.g., Allen et al., 1989). Since then, some researchers (e.g., Kappenman, 2012) have suggested that the power grid systems of the United States, and of the northeast, in particular, might be vulnerable to the future arrival of a rare magnetic superstorm, possibly causing a widespread and long-lasting interruption of electric power transmission that would carry significant economic cost (Abt Associates, 2017; Baker et al., 2008; Barnes & Van Dyke, 1990; Lloyd's of London, 2013).

Qualitatively, the physical connection between magnetic storms and interference to power grid systems is understood: Geoelectric fields induced in the Earth's conducting interior drive uncontrolled, quasi-direct currents through power grid grounding connections (e.g., Molinski, 2002; Piccinelli & Krausmann, 2014; Samuelsson, 2013). Two factors conspire together to produce spatially complex geoelectric fields across the Northeast United States. First, the northeast is situated at latitudes that are close to the ionospheric current

systems of the auroral zone, and, therefore, local storm time geomagnetic activity can be intense and complicated (e.g., Prölss, 2004, chapter 8.3.1)—at any instant in time, it can be of high amplitude in some locations, and of lower amplitude in others (e.g., Ngwira et al., 2015; Pulkkinen et al., 2015). Second, the geology of the northeast is complicated (e.g., Rast, 1989; Roy, 1987), and, therefore, subsurface Earth conductivity structure is complicated as well (e.g., Murphy & Egbert, 2017; Ogawa et al., 1996). Synthetic calculations for other geological settings have shown that subsurface structure can support the induction of geoelectric fields having a high degree of geographic granularity, with high amplitude in some places and low amplitude in others, as well as very different degrees of geoelectric polarization (e.g., Bedrosian & Love, 2015; McKay & Whaler, 2006). In light of all of this, one can anticipate that obtaining accurate estimates of geoelectric hazards across the northeast is bound to be a technical challenge.

In estimating northeastern geoelectric hazards, we rely on geophysical measurements and simple derivatives and integrations of those measurements. Our methods build on those developed by Love et al. (2018a, 2018b) and Lucas et al. (2018) in their analyses of the Mid-Atlantic and Pacific Northwest United States. We estimate (retrospectively) geoelectric time series by convolving magnetotelluric impedance tensors obtained for various survey sites with geomagnetic time series acquired over decades of time at three magnetic observatories that straddle the geographic extent of the northeast. From statistical analysis of these geoelectric time series, we construct maps of extreme-value geoelectric amplitude and extreme-value polarization. We interpret these new results in terms of regional geological structures. Results inform projects for assessing the vulnerability of power grid systems to geomagnetic disturbance, mandated by the United States Federal Energy Regulatory Commission, (2013, Order No. 779). Geoelectric polarization is an important variable for estimating voltages and currents induced on power grid lines during magnetic storms, but it has not generally been highlighted in hazard analyses—polarization is not examined, for example, in the "100-year benchmark" analysis of NERC (2014). Our results concerning both extreme-event amplitude and polarization contribute to a larger enterprise for developing "benchmark" intensity estimates for extreme space weather events (National Science and Technology Council, 2015, Goal 1.1).

## 2. Induction in the Conducting Earth

A practical way to estimate storm-time geoelectric fields across a given geographic region is through a parameterization of induction that uses estimates of Earth-surface impedance, dervied from magnetotelluric survey measurements, and time series of geomagnetic variation, acquired at magnetic observatories. As part of a magnetotelluric campaign (e.g., Chave & Jones, 2012; Simpson & Bahr, 2005; Unsworth, 2007), measurements (e.g., Ferguson, 2012) are made of the time ($t$)-varying geomagnetic $\mathbf{B}(t,x,y)$ and geoelectric $\mathbf{E}(t,x,y)$ fields at various geographic locations (north $x$, east $y$). Conventionally, the relationship between variation in the horizontal geomagnetic $\mathbf{B}_h = [B_x, B_y]$ and geoelectric, $\mathbf{E}_h = [E_x, E_y]$ field components is parameterized in terms of a linear equation, one that is conveniently treated in the frequency domain,

$$\mathbf{E}_h(f,x,y) = \frac{1}{\mu}\mathbf{Z}(f,x,y)\cdot\mathbf{B}_h(f,x,y), \tag{1}$$

where $f$ is Fourier frequency (period $T = 1/f$), $\mu$ is magnetic permeability, and $\cdot$ denotes multiplication. The impedance tensor,

$$\mathbf{Z}(f,x,y|\sigma(\mathbf{r})) = \begin{bmatrix} Z_{xx} & Z_{xy} \\ Z_{yx} & Z_{yy} \end{bmatrix}(f,x,y|\sigma(\mathbf{r})), \tag{2}$$

is $2\times 2$ and complex (real and imaginary; e.g., Weidelt & Chave, 2012). With inverse Fourier transformation of equation (1), induction can be described in the time domain as

$$\mathbf{E}_h(t,x,y) = \frac{1}{\mu}\left(\mathbf{Z} * \mathbf{B}_h\right)(t,x,y), \tag{3}$$

where, in this equation, $\mathbf{Z}(t)$ is the impedance impulse response function (e.g., Egbert, 1992; Kelbert et al., 2017) and $*$ denotes convolution. Impedance has units of $\Omega$ (ohms); the Earth's surface impedance is a nonlinear function of the electrical conductivity structure beneath the surface, $\sigma(\mathbf{r})$ (or, equivalently, subsurface resistivity structure, $\rho(\mathbf{r}) = 1/\sigma$), where $\mathbf{r}$ is the position vector. The bulk electrical conductivity of a rock, taken from a given location on or within the Earth, can differ by orders of magnitude from the conductivity of another rock taken from a different location. Indeed, rock conductivity is a function of many ancillary

properties, including mineralogy, melt and solid phases, water and clay content, porosity, cracks, and grain boundaries (e.g., Evans, 2012; Yoshino, 2011). Seawater is a good electrical conductor, and, near the coasts, the oceans can affect Earth surface impedance.

Although the impedance tensor (2) can be empirically estimated from electromagnetic measurements made at the surface, the parameterizations given by (3) and (1) are theoretically justified under two important assumptions. First, for the variational frequencies $f$ of interest, the classical laws of "quasi-static" electromagnetism apply for induction within the Earth, and Maxwell's displacement currents are ignored (e.g., Stratton, 1941, Chapter 5). This means that electromagnetic field variation in the Earth can be described by the diffusion equation, and, in particular, for a bulk resistivity $\rho$, field amplitudes are attenuated with characteristic depth and lateral length scales given by

$$\delta(f) = \sqrt{\frac{\rho}{\pi\mu f}} \quad \text{or} \quad \delta[\text{m}] \approx 500\sqrt{\rho[\Omega - \text{m}] \cdot T[\text{s}]}. \tag{4}$$

Second, the plane-wave approximation applies (Wait, 1982, Chapter VI), under which electromagnetic field variation generated by the space weather above the Earth's surface must have a characteristic horizontal surface length scale $L(f)$ that is longer than the corresponding diffusive scale; that is,

$$\delta(f) < L(f). \tag{5}$$

Using many empirical impedance tensors estimated (e.g., Chave, 2012; Egbert, 2007a) from magnetotelluric measurements made at different locations as part of a survey, models of Earth conductivity structure can be obtained through inversion (e.g., Egbert, 2007b; Rodi & Mackie, 2012). Qualitatively, the Earth's internal structure is revealed in the relative symmetry (or asymmetry) of the impedance tensor, which is conveniently explored in the frequency dependence of "apparent" resistivity and the phase relationship between the geomagnetic and geoelectric field variation, given, respectively, by

$$\rho_{jk}(f) = \frac{\left|Z_{jk}(f)\right|^2}{2\pi\mu f} \text{ and } \phi_{jk} = \tan^{-1}\left[\frac{\text{Im}(Z_{jk})}{\text{Re}(Z_{jk})}\right] \tag{6}$$

(e.g., Berdichevsky & Dmitriev, 2008, p. 10). In section 5, we use equation (1) for forward calculation—frequency domain multiplication (or time domain convolution) of survey magnetotelluric impedance tensors $\mathbf{Z}$ with records of geomagnetic variation $\mathbf{B}_h$ acquired at observatories to calculate geoelectric variation $\mathbf{E}_h$ (e.g., Bonner & Schultz, 2017; Kelbert et al., 2017; Pirjola, 2002; Weigel, 2017). However, in light of equation (5), we recognize that we need to be cautious in interpreting geoelectric fields calculated from geomagnetic time series acquired at observatories that are far removed from the local estimates of impedance.

We have previously used similar empirically based methods in analyzing geoelectric hazards for other parts of the continental United States (e.g., Love et al., 2018a, 2018b; Lucas et al., 2018). Our methods stand in distinct contrast to analyses of geoelectric hazards (e.g., Gannon et al., 2012; Marti et al., 2014; NERC, 2014; Ngwira et al., 2015; Pulkkinen et al., 2015; Nikitina et al., 2016; Trichtchenko et al., 2016; Wei et al., 2013) relying on idealized models for broad regions of the Earth with structure that is simply depth dependent, one-dimensional (e.g., Blum et al., 2015; Ferguson & Odwar, 1997; Fernberg, 2012). For such models, surface impedance has the symmetric form

$$\mathbf{Z}_{1\text{D}}(f, x, y|\sigma(\mathbf{r})) = \begin{bmatrix} 0 & Z \\ -Z & 0 \end{bmatrix}(f, x, y|\sigma(\mathbf{r})), \tag{7}$$

for which $\rho_{xy} = \rho_{yx}$, and $\rho_{xx} = \rho_{yy} = 0$. In such an idealized Earth model, induced geoelectric fields of a particular frequency are always orthogonal to the inducing geomagnetic field. For an (even more idealized) Earth model consisting of a uniformly conducting half-space, $\phi_{xy} = \phi_{yx} = 45°$. Caution is warranted in using one-dimensional models—magnetotelluric surveys already demonstrate that Earth surface impedance has a high degree of geographic granularity, and this can affect the local amplitude, polarization, and phase of geoelectric fields in ways that are inconsistent with regional models having one-dimensional impedances (e.g., Bedrosian & Love, 2015; Bonner & Schultz, 2017).

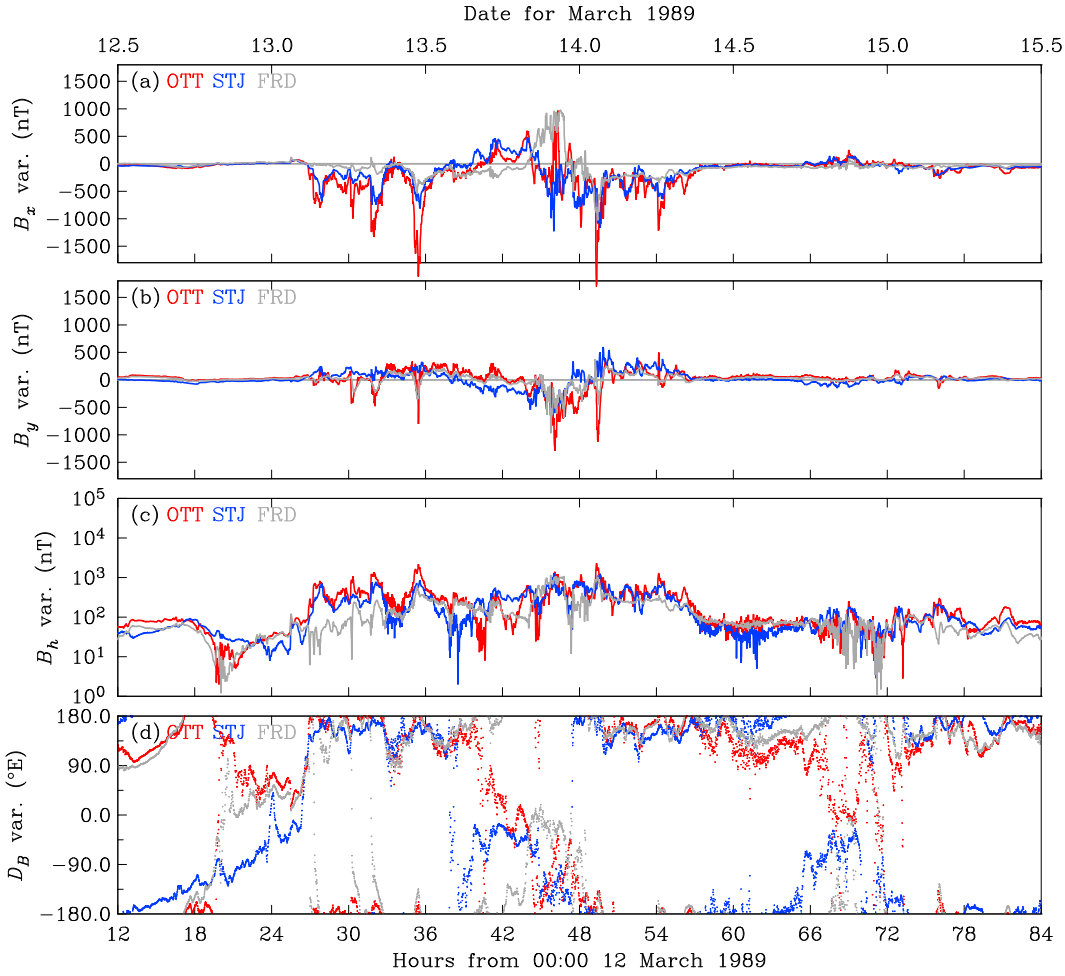


**Figure 1.** Time series of 1-min resolution geomagnetic (a) north $B_x(t_i)$ variation (baseline removed), (b) east $B_y(t_i)$ variation, (c) horizontal intensity $B_h(t_i)$ variation, and (d) geomagnetic declination variation $D_B(t_i)$ recorded at OTT (red), STJ (blue), and FRD (gray) during the storm of March 1989.

## 3. Magnetic Observatory Time Series

For $\mathbf{B}_h$, we use 1-min resolution, definitive-quality magnetometer time series acquired at three magnetic observatories: for years 1979–2016, from the Natural Resources Canada observatories at Ottawa (OTT), Ontario (geographic: 45.40°N, 75.55°W; 2000 geomagnetic: 55.63°N, 4.97°W), and the Saint John's (STJ), Newfoundland observatory (geographic: 47.59°N, 52.68°W; 2000 geomagnetic: 57.15°N, 23.83°E; Newitt & Coles, 2007); for years 1983–2016, from the U.S. Geological Survey (USGS) observatory at Fredericksburg (FRD), Virginia (Love & Finn, 2011; U.S. Geological Survey, 1901; geographic: 38.20°N, 77.37°W; 2000 geomagnetic: 48.41°N, 6.89°W). The OTT and STJ observatories are situated on similar (typically, subauroral) geographic and geomagnetic latitudes, but they are separated, mostly in longitude, by 1,761 km; the FRD observatory is a midlatitude observatory located 814 and 2,251 km from OTT and STJ, respectively. Vector data from each observatory are recorded as discrete values $\mathbf{B}_h(t_i)$ for a time stamp sequence $t_1, t_2, t_3, \ldots$, with a 1-min $= t_i - t_{i-1}$ sampling interval (2-min or 120-s Nyquist). As an example, in Figures 1a and 1b, we plot 1-min $\mathbf{B}_h(t_i)$ variational time series (a constant baseline has been subtracted) recording the $Kp = 9$ magnetic storm of March 1989 at OTT, STJ, and FRD; in Figures 1c and 1d, we plot 1-min variation of the horizontal intensity variation, $B_h(t_i) = \sqrt{(B_x(t_i) - B_x^0)^2 + (B_y(t_i) - B_y^0)^2}$, and declination variation (horizontal direction), $D_B(t_i) = \tan^{-1}\left[(B_y(t_i) - B_y^0)/(B_x(t_i) - B_x^0)\right]$, where $[B_x^0, B_y^0]$ is a time steady baseline. The storm commenced at 01:28 UT on 13 March, and it reached a maximum $-Dst = 589$ nT at 01:30 UT on 14 March.

We see from Figure 1 that, over the course of the March 1989 storm, geomagnetic variation is only roughly correlated between recordings from the three observatories. Differences in geomagnetic variation recorded

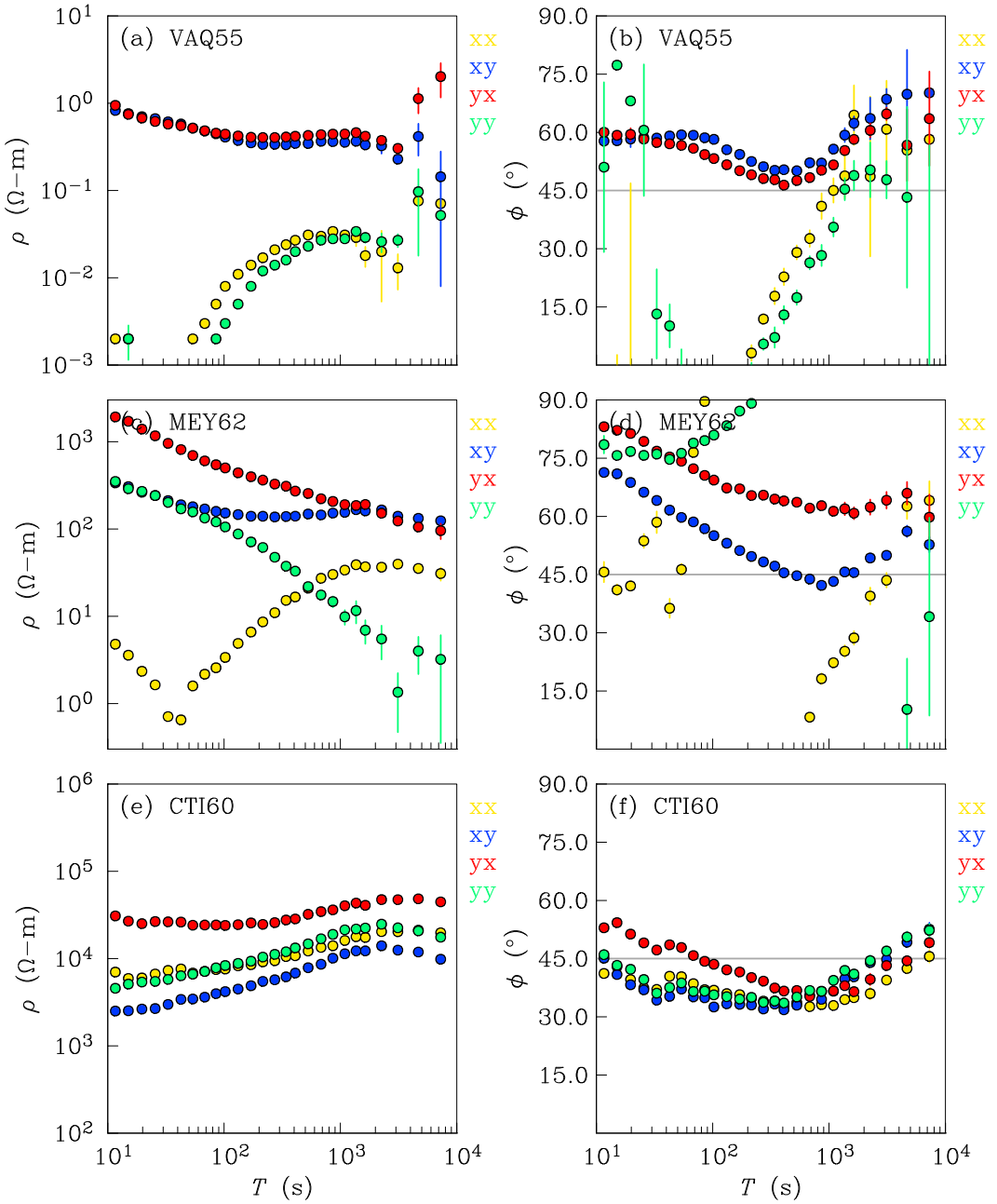


**Figure 2.** Apparent resistivities and phases, $\rho_{xx}(T), \phi_{xx}(T)$ (yellow); $\rho_{xy}(T), \phi_{xy}(T)$ (blue); $\rho_{yx}(T), \phi_{yx}(T)$ (red); and $\rho_{yy}(T), \phi_{yy}(T)$ (green), together with one standard deviation error bars, each plotted as a function of variational period $T$, for EarthScope survey sites (a, b) VAQ55, (c, d) MEY62, and (e, f) CTI60.

at the three observatories represent inconsistencies with the plane-wave assumption; they are due to localized and transient structures in storm time ionospheric and magnetospheric current systems at heights greater than ~100 km. With geometric attenuation, the horizontal length scale characterizing ground-level geomagnetic variation generated by these currents will generally exceed 100 km. Empirical analysis of 1-min, horizontal-component geomagnetic variation recorded by high-latitude magnetometers shows that there is good coherence in signals separated by ~200 km (Watermann et al., 2006). Recognizing that the northeast is a midlatitude setting, and bearing equation (5) in mind, then, we can infer that for periods greater than 1 min, 200 km $< L <$ 814 km; where the upper bound, here, is the minimum distance between the three observatories.

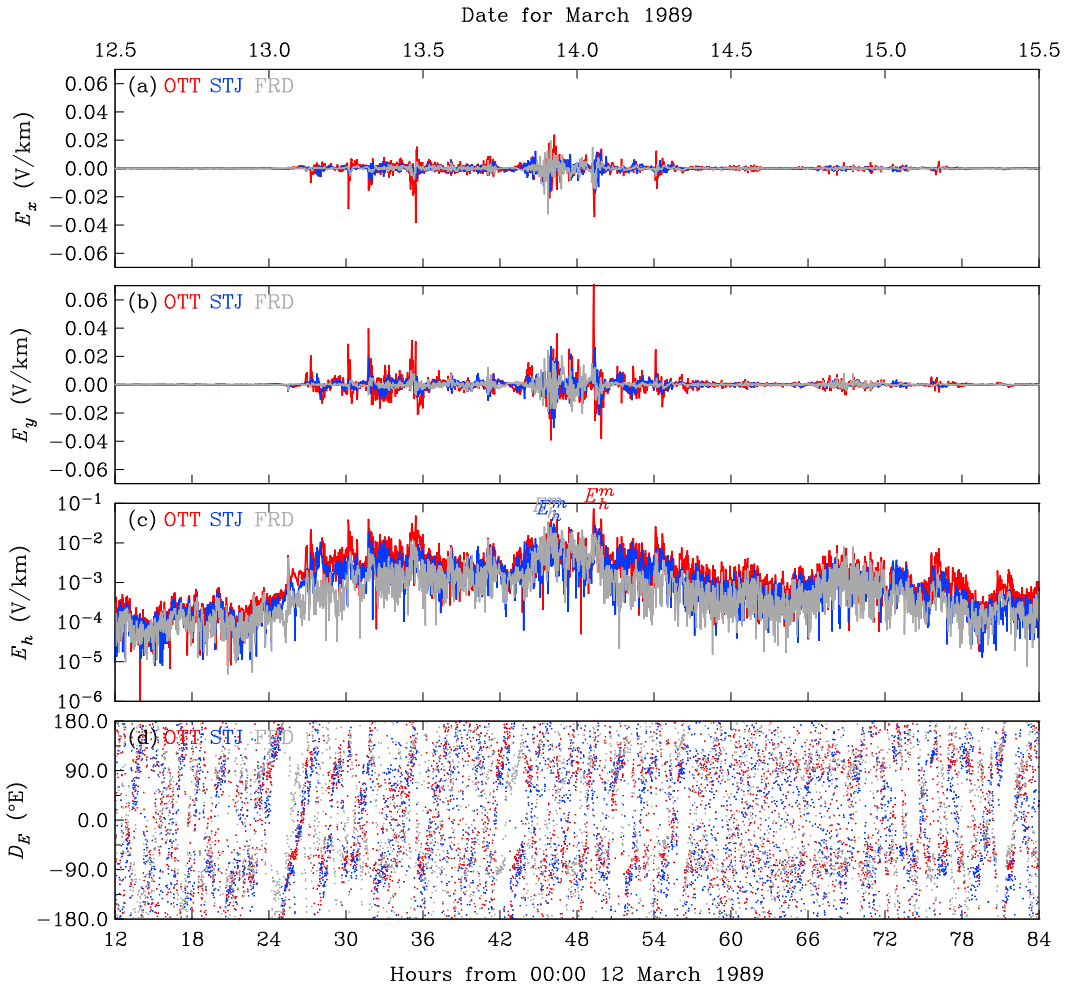


**Figure 3.** Time series of 1-min resolution geoelectric (a) north $E_x(t_i)$ and (b) east $E_y(t_i)$ field components, (c) horizontal intensity $E_h(t_i)$, and (d) absolute geoelectric declination $D_E(t_i)$ for OTT (red), STJ (blue), and FRD (gray) geomagnetic induction at survey site VAQ55 during the storm of March 1989.

## 4. Magnetotelluric Impedance Tensors

For **Z**, we use 172 magnetotelluric impedance tensors acquired from measurements made at survey sites (Schultz, 2010; Schultz et al., 2006) across the Northeast United States between 2014 and 2017 as part of the National Science Foundation's EarthScope project (Williams et al., 2010). With a nominal spacing of 70 km, the survey sites extend over the northeast from Maine in the north down to 35.33°N (most of North Carolina) and west to 81.40°W (most of West Virginia). Each tensor $\mathbf{Z}\left(f_i, x, y\right)$ for each site $(x, y)$ is parameterized for a discrete set of frequencies, $f_1, f_2, f_3, \ldots$ within the band from $10^{-4}$ to $10^{-1}$ Hz (periods of 10,000 to 10 s); typical errors are estimated to be less than 5% (Schultz, 2010). The EarthScope database includes a quality rating assigned to each tensor (Kelbert et al., 2011): 5 ("excellent"), 4 ("good"), 3 ("fair"), etc.; tensors with ratings of 3 or higher are suitable for our work here.

To interpret the impedance tensors, in Figure 2, we plot apparent resistivities $\rho_{jk}(T)$ and phases $\phi_{jk}(T)$, each as a function of variational period, and for three different EarthScope tensors. The site denoted VAQ55 is in western Virginia (37.88°N, 79.81°W) and located on conductive sedimentary rock near the edge of the Appalachian Basin (e.g., Virginia Division of Mineral Resources, 1993). For geomagnetic variation with a period of 100 s, apparent resistivity at this site is ~ 0.5 Ω-m, with induction occurring, primarily, in the upper crust and across diffusive scales of ~3.5 km. From Figure 2a, we see that for variation from 10 to about 100 s, $\rho_{xy} \approx \rho_{yx}$, while both $\rho_{xx}$ and $\rho_{yy}$ are much smaller, and $\phi_{xy} \approx \phi_{yx}$. These simple observations, for these variational periods, indicate structure beneath and surrounding this site that is close to being one-dimensional, depth dependent. Asymmetry is seen for variation at periods greater than 100 s. At periods of 10,000 s, appar-

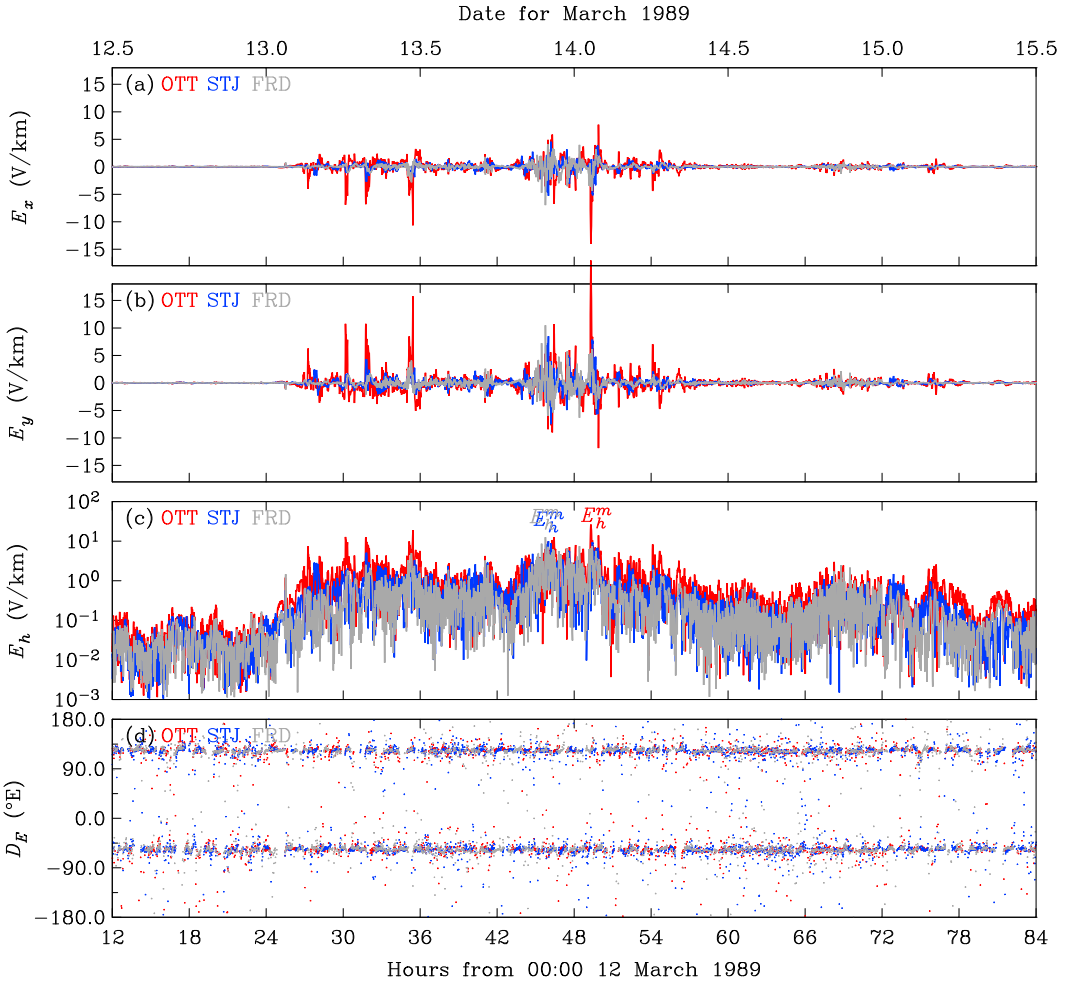


**Figure 4.** Time series of 1-min resolution geoelectric (a) north $E_x(t_i)$ and (b) east $E_y(t_i)$ field components, (c) horizontal intensity $E_h(t_i)$, and (d) absolute geoelectric declination $D_E(t_i)$ for OTT (red), STJ (blue), and FRD (gray) geomagnetic induction at survey site CTI60 during the storm of March 1989.

ent resistivity is ~2.0 Ω-m, with induction occurring across the lower crust with diffusive scales of ~70.7 km. So, for this site, and across the variational periods of 100 to 10,000 s, 3.5 km $< \delta <$ 70.7 km.

The situation is very different for MEY62, a site in northern Maine (46.98°N, 67.88°W) located on weakly metamorphosed marine sandstone and slate (e.g., Loiselle, 2002). In Figure 2c, we see considerable asymmetry in apparent resistivity and phase. From 10 to 1,000 s, $\rho_{xy} \neq \rho_{yx}$, and from 10 to 100 s, $\rho_{yy} \approx \rho_{xy}$, indicating structure beneath and surrounding the site that is far from simply depth dependent, one-dimensional. For this site, and across the variational periods of 100 to 10,000 s, 100 km $< \delta <$ 500 km. Site CTI60 in the western highlands of Connecticut (north of New York City, 41.79°N, 73.32°W) is located on resistive metamorphic and igneous bedrock of the crystalline Appalachians (e.g., Connecticut Geological Survey, 2013). In Figure 2e, from 10 to 10,000 s, $\rho_{xy} \neq \rho_{yx}$, indicating structure beneath and surrounding the site that is evidently far from simply depth dependent, one-dimensional. For this site, and across the variational periods of 100 to 10,000 s, 700 km $< \delta <$ 9,000 km.

## 5. Geoelectric Time Series

For each of the 172 magnetotelluric survey sites across the Northeast United States and for geomagnetic variation recorded at each of OTT and STJ (1979–2016), and FRD (1983-2016), we use an algorithm to calculate induction—fast Fourier transformation of detrended geomagnetic time series into the frequency domain, multiplication with impedance tensor, per equation (1), and inverse transform back into the time domain—to obtain estimated geoelectric time series (Love et al., 2018a; Lucas et al., 2018); since we use

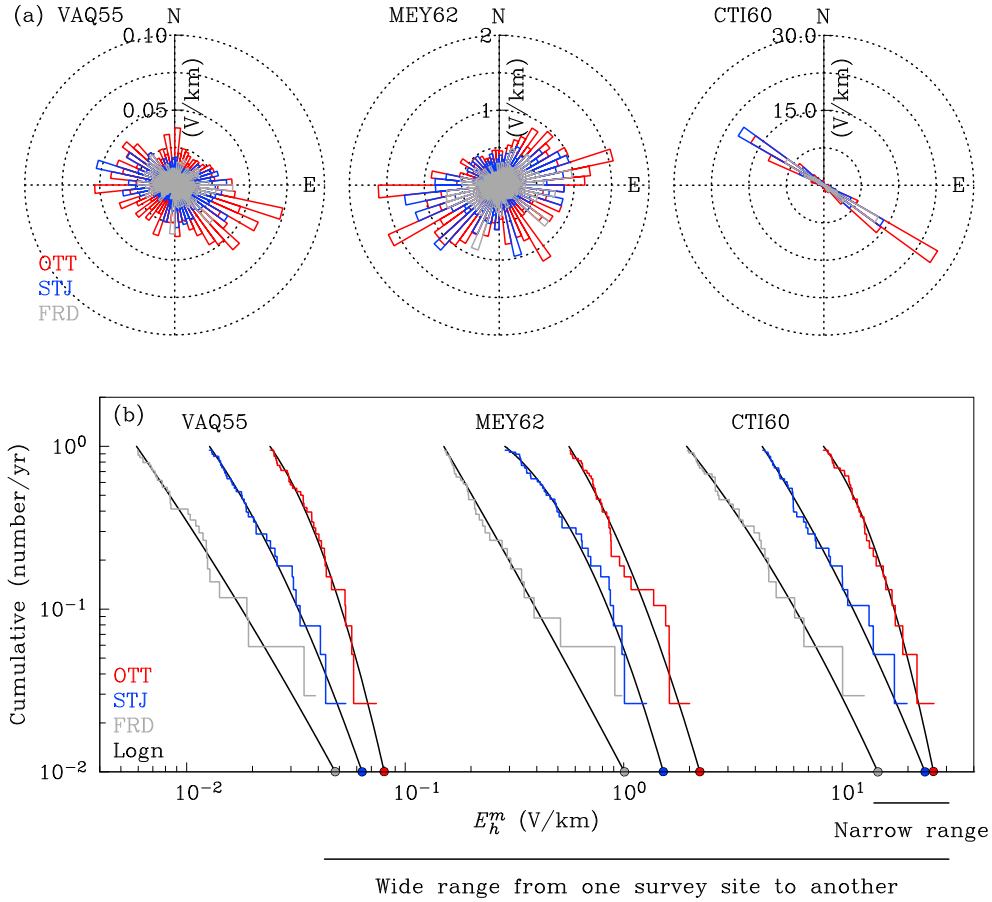


**Figure 5.** Polar plots (a) of maximum geoelectric amplitude binned in declination as realized at survey sites VAQ55, MEY62, and CTI60 for induction driven by geomagnetic variation at OTT (red), STJ (blue), and FRD (gray), each for years 1983–2016. Cumulative number (b) of times per year that storm-maximum amplitude exceeds the threshold $E_h^m$ calculated for EarthScope survey sites VAQ55, MEY62, CTI60, each for OTT (red, 1979–2016), STJ (blue, 1979–2016), and FRD (gray, 1983–2016), together with fitted lognormal statistical models (black). The intersections of the models with the horizontal axes, indicated by dots, amount to extrapolated 100-year threshold values, $E_h^{100}$.

1-min resolution geomagnetic time series, the geoelectric time series $\mathbf{E}_h(t_i, x, y)$ are limited to 1-min resolution as well. In Figures 3a and 3b, we plot these geoelectric time series for the March 1989 storm for survey site VAQ55, for induction driven by geomagnetic variation at all three observatories; in Figures 4a and 4b, we plot corresponding results for survey site CTI60. With comparison against Figures 1a and 1b, we see that, during this storm, variance in the geoelectric time series is, at both sites, generally high (low) when geomagnetic activity is high (low), but there are also obvious differences.

In Figures 3c and 4c, we plot time series of the absolute geoelectric amplitude, $E_h(t_i) = \sqrt{E_x^2 + E_y^2}$ for sites VAQ55 and CTI60; here too, correlation between the three time series is obvious, but differences, in detail, can also be readily seen. At site VAQ55, the storm time maxima $E_h^m$ for the OTT, STJ, and FRD time series occurred at different times: at 01:17 UT on 14 March, 22:10 on 13 March, and 21:45 on 13 March, with values of 0.07, 0.03, and 0.03 V/km, respectively. For site CTI60, the maxima $E_h^m$ are of much higher amplitude, for the OTT, STJ, and FRD time series they occurred at 01:17 UT on 14 March, 21:59 on 13 March, and 21:46 on 13 March, with values of 26.31, 10.01, and 12.60 V/km. For perspective, prior to these maximum geoelectric amplitudes, numerous northeastern and mid-Atlantic electric power companies had already noted operational anomalies (NERC, 1990), and to the north, the Hydro-Québec collapse occurred at 07:45 on 13 March, which was also prior to the maximum geoelectric amplitudes seen in Figures 3c and 4c.

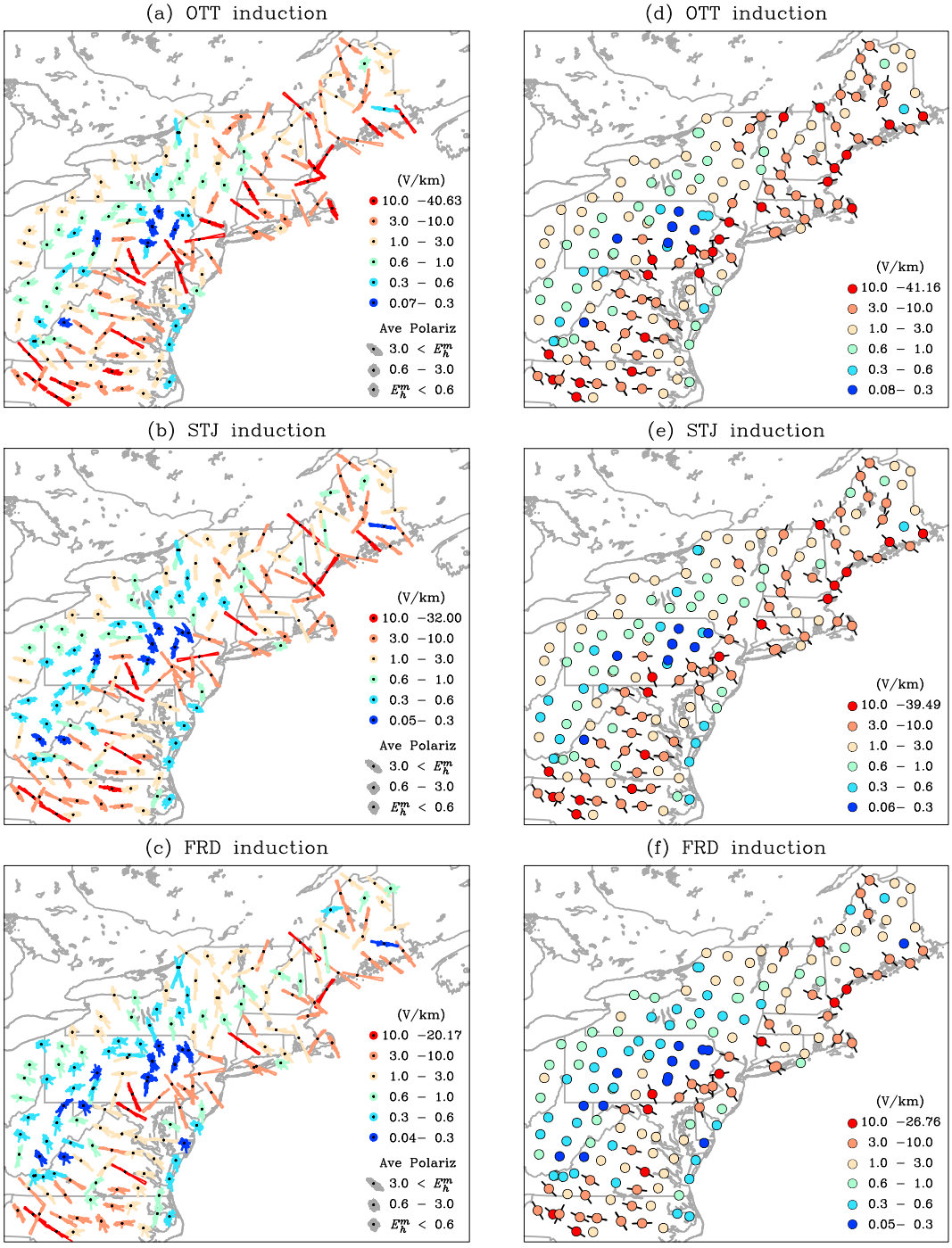


**Figure 6.** Maps showing polar plots of declination-binned maximum geoelectric amplitude for all 172 survey sites for (a) OTT, (b) STJ, and (c) FRD induction, each color coded for maximum amplitude for 1983–2016; also shown are average polarizations (gray) for the northeast; 100-year geoelectric amplitudes $E_h^{100}$ and most likely declination axes (for sites with $E_h^{100} > 3.0$ V/km) or (d) OTT, (e) STJ, and (f) FRD induction.

In Figures 3d and 4d, we plot geoelectric declination, $D_E(t_i) = \tan^{-1}\left[E_y/E_x\right]$. Here we see that the geoelectric field for site VAQ55 is not especially polarized, while for site CTI60 it is strongly polarized, with $D_E(t_i) \approx -57°/123°\text{E}$. For both sites, the degree of polarization is not tightly tied to the level of geomagnetic activity (Figures 1b and 1d); so, in particular, the geoelectric field at CTI60, Figure 4d, is polarized both before storm commencement and during the storm. From these simple observations, we might conclude that geoelectric polarization is mostly the result of induction in subsurface Earth structure. Some of this might have been anticipated upon consideration of the apparent resistivities and phases at each site. Consider, first, the relatively one-dimensional setting of VAQ55. Even as geomagnetic variation rather slowly courses around in direction, Figure 1d, the impedance at VAQ55, with $\phi_{xy} \neq \phi_{yx}$, Figures 2a and 2b, causes a broad elliptical cycling of the geoelectric field, with geoelectric declination rapidly sweeping across meridional angles, Figure 3d,. On the other hand, at CTI60, even though $\phi_{xy} \neq \phi_{yx}$, the extreme asymmetry in the local impedance, $\rho_{xy} < \rho_{xx} \approx \rho_{yy} < \rho_{yx}$, Figures 2e and 2f, causes the induced geoelectric field to be tightly polarized (Figure 4d).

For a given survey site, differences between the geoelectric time series calculated for induction from the OTT, STJ, and FRD observatories are due to localized nonplane-wave differences in geomagnetic variation recorded at each observatory—indeed, from discussion in sections 3 and 4 we understand that the plane-wave condition given by equation (5) is not always satisfied, and, furthermore, that the distance between the three observatories exceeds the horizontal length scale $L$ characterizing horizontal geomagnetic field variation. This means that it would be a challenge to map geoelectric field variation over the course of (say) an individual magnetic storm using geomagnetic time series data from the three observatories. But this is not our objective here. Instead, our focus is on the statistical analysis of extreme-value geoelectric amplitudes and declinations. The sensitivity of our statistical results to the use of geomagnetic data from three widely separated observatories is something we examine in sections 6 and 7.

## 6. Maps of Amplitude and Declination

To investigate the relationship between the amplitude and declination of geoelectric field variation, for each magnetotelluric survey site and for induction driven by geomagnetic variation at OTT, STJ, and FRD (for consistency, each for years 1983–2016), we identify the maximum geoelectric amplitude $E_h(t_i, x, y)$ within 6° wide bins of geoelectric declination $D_E$. In Figure 5a, we plot example results as polar diagrams for sites VAQ55, MEY62, and CTI60; in Figure 5b, we plot, each on the same axis, the cumulative number of occurrences per year that exceed $E_h^m$ for the same sites. Geoelectric amplitudes are generally highest for OTT induction and lowest for FRD induction; the proportion in amplitudes between induction for these two observatories is about a factor of 2. Of the three sites, amplitudes and the degree of (declinational) polarization are lowest at VAQ55 and highest at CTI60; the amplitude proportion between these two survey sites is about a factor of 350. It is noteworthy that polarization differs from one site to another—compare results for VAQ55 and CTI60 with that for MEY62.

In Figures 6a–6c, we give summary maps for all 172 survey sites, each for OTT, STJ, and FRD induction, and color coded for the maximum amplitude at each site for 1983–2016; see supporting information for numerical values. From these maps, we recognize immediately that the range in geoelectric amplitude from one survey site to another is greater than the differences at any given survey site between induction driven by geomagnetic variation recorded at any one of OTT, STJ, and FRD. Apparently, the statistical parameters describing geoelectric amplitude and declination, estimated from many storms, are insensitive to nonplane-wave geomagnetic variation, such as would be realized during the time evolution of an individual magnetic storm. The primary factor affecting the geographic granularity seen in Figures 6a–6c is site-to-site differences in solid-Earth surface impedance. Therefore, we can reasonably interpolate the geoelectric amplitude (we interpolate the logarithm of amplitude, binned in declination); recognizing that geomagnetic activity tends to be organized in geomagnetic latitude, we interpolate linearly across the longitudes of OTT and STJ and then, separately, across the average latitude of OTT-STJ and the latitude of FRD; we show maps of these interpolated results in Figure 7a; see supporting information for numerical values .

We call attention to the fact, evident from Figures 6a–6c and 7a, that geoelectric fields tend to be most (least) polarized at locations with high (low) geoelectric amplitude. This tendency can be highlighted by averaging the declination-binned amplitudes from all northeastern sites within amplitude bands; we show these results in the lower-right-hand corner of Figures 6a–6c and 7a. For sites realizing maximum

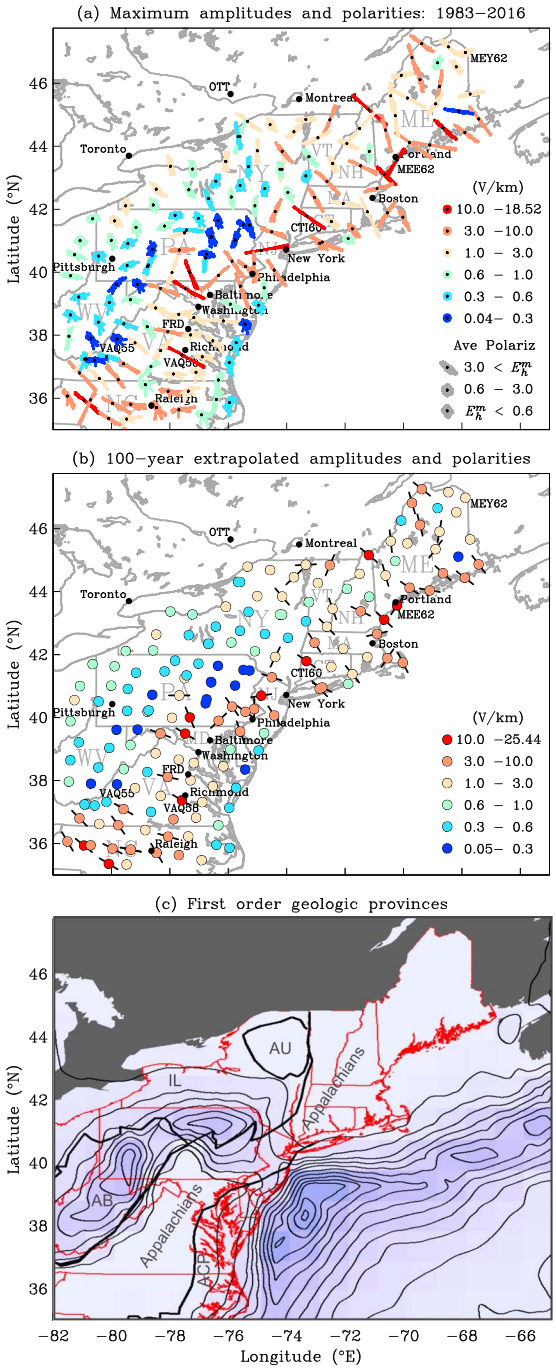


**Figure 7.** Maps showing (a) polar plots of interpolated declination-binned maximum geoelectric amplitude for all 172 survey sites, each color coded for maximum amplitude for 1983–2016; also shown are average polarizations (gray) for the northeast; (b) interpolated $E_h^{100}$ and most likely declination axes (for sites with $E_h^{100} > 3.0$ V/km); (c) first-order geologic provinces across the northeast, along with 1-km contours of estimated sediment thickness; Appalachian Basin (AB), Appalachian Coastal Plane (ACP), Adirondack Uplift (AU), and Interior Lowlands (IL). Blue colored background indicates sediment thickness from Laske and Masters (1997). A filtered version of the sediment thickness data are shown as 1-km contours.

$E_h > 3.0$ V/km at one time or another over the past several decades, the average polarization is clearly southeast-to-northwest, while for sites with more modest maximum $E_h$, such as for either of the bands 0.6–3.0 V/km or $E_h < 0.6$ V/km, polarization does not show a distinctive preferred direction. It is worth emphasizing that the polarization results, shown in Figures 6a–6c and 7a, cannot be reproduced using impedances derived from one-dimensional Earth conductivity models (Blum et al., 2015; Ferguson & Odwar, 1997; Fernberg, 2012), such as those used to estimate benchmarks for NERC (2014).

## 7. One Hundred-Year Extrapolations

We analyze the statistics of 1-min extreme-value geoelectric amplitudes $E_h(t_i, x, y)$ at the various magnetotelluric survey sites. For this, we use an algorithm (described in ; Love et al., 2018a) that identifies and keeps, for statistical analysis, the maximum amplitude $E_h^m$ for each period of magnetic storm disturbance. We analyze the $N$ largest $E_h^m$ amplitudes at each site. For consistency between geoelectric time series of different length (the FRD time series, 1983–2016, are longer than those for OTT and STJ, 1979–2016), we chose $N$ equal to the number of years in each time series; this leaves us with an average of one extreme $E_h^m$ value per year. We hypothesize, as often done in analyzing the amplitudes of space weather measurables (e.g., Burlaga & Lazarus, 2000; Riley & Love, 2017; Yurchyshyn et al., 2005), that $E_h^m$ values are realized from a lognormal distribution (e.g., Love et al., 2015, 2018a; Pulkkinen et al., 2012), such as would be appropriate for a statistical process resulting from the multiplication of numerous random, positive variables (e.g., Chave, 2017, Chapter 3.4.4). In summary, solar activity can be modeled as autoregressive dynamo action (e.g., Solanki et al., 2002); the geoeffectiveness of solar wind-magnetosphere coupling is determined by the multiplicative action of solar wind velocity, density, and interplanetary magnetic field (e.g., Newell et al., 2007), measurements of some of these variables are, themselves, lognormally distributed (e.g. Asaoka et al., 2003; Veselovsky et al., 2010), and the evolution of a magnetic storm can be modeled as an autoregressive process (e.g., Vassiliadis et al., 1999). All of this, together, suggests that a lognormal process is a plausible hypothesis for modeling geoelectric amplitudes. As noted by Love et al. (2018a), the use of a lognormal model will, generally, give extrapolations to more extreme-value amplitudes than those obtained using a power law model, and, in that sense, our use for the lognormal model can be considered "conservative." Using a maximum-likelihood algorithm, we fit lognormal functions to the $E_h^m$ for each survey site, and each for OTT and STJ (1979–2016), and FRD (1983–2016) induction. In Figure 5b, we plot the cumulatives of the fitted lognormal functions. These fits are reasonably good representations of the data; Kolmogorov-Smirnov $p$ value—corrected for bias (e.g., Chave, 2017; Steinskog et al., 2007), median values from multiple bootstrap resamplings—are too large (generally, $> 0.20$) to objectively permit simple rejection of the lognormal hypothesis.

Since it is physically plausible provides good fits to geoelectric amplitudes, we use the lognormal model to extrapolate to threshold values that are only exceeded, on average, once per century, $E_h^{100}$. As might be expected, these extrapolations are similar for OTT and STJ induction (the two observatories are on similar latitudes); among the survey sites in the northeast, on average, the OTT 100-year extrapolations are 1.26 times higher than that those for STJ. Remarkably, however, because the FRD distributions are relatively flat, the 100-year extrapolations for geoelectric exceedance for FRD induction approach those for OTT and STJ—the intersections of the lognormal functions with the horizontal axis in Figure 5b are closely spaced—the OTT (STJ) extrapolations are 1.76 (1.49) times higher than for FRD. We speculate that the reason the FRD distribution is flatter than those for OTT and STJ is related to the fact that during high levels of geomagnetic activity, the auroral zone broadens in latitude and, to some extent, slips slightly south. So while high-latitude observatories, such as OTT and STJ, frequently experience auroral-zone levels of activity, midlatitude observatories, such as FRD, only occasionally experience auroral-zone levels of activity. The net effect is to flatten out the distribution characterizing midlatitude activity. With respect to extrapolation errors, we note from Figure 5b that, for each survey site, differences in estimated $E_h^{100}$ values for induction between OTT, STJ, and FRD are much smaller than the more than 2 orders of magnitude range in $E_h^{100}$ seen, for example, between the survey sites VAQ55 and CTI60.

In Figures 6d–6f, we show maps of 100-year geoelectric amplitudes $E_h^{100}$ and most likely declination axes (for $E_h^{100} > 3.0$ V/km) for all 172 survey sites, each for OTT, STJ, and FRD induction. As with our observations given in section 7 for Figures 6a–6c, the 100-year amplitudes shown in Figures 6d–6f, extrapolated from geoelectric amplitudes realized for many storms, are apparently insensitive to nonplane-wave geomagnetic variation, such as would be realized during an individual magnetic storm. Again, the primary factor affecting the geographic granularity seen in Figures 6d–6f is site-to-site differences in solid-Earth surface

impedance. Therefore, we can reasonably interpolate the statistical extrapolations of 100-year geoelectric amplitudes obtained for geomagnetic variation at each observatory. In Figure 7b, we give corresponding maps for 100-year amplitudes and most likely declinations, interpolated across the geomagnetic longitudes and separately across the latitudes of the three observatories; see supporting information for numerical values . As noted, there is, on average, a proportion of 1.76 between OTT and FRD $E_h^{100}$ values (the two observatories are at different latitudes). Interpolation across latitudes gives estimated geoelectric amplitudes that roughly split this proportionality, and so we estimate that our interpolated $E_h^{100}$ have "errors" of about 38%. And while this might, at first, seem large, as already noted, it is much smaller than the more than 2 orders of magnitude range in $E_h^{100}$ seen among the various survey sites. Our estimate of the error left after interpolation is comparable to the statistical errors inherent to the 100-year extrapolation that Love et al. (2018a) estimated using a bootstrap resampling method (e.g., Efron & Tibshirani, 1993).

Among the various survey sites, our estimated 100-year amplitudes exceed 10 V/km at 10 of the 172 sites; they exceed 3 V/km at 48 of the sites; and they exceed 1 V/km at 95 sites (or 55% of the sites). In more detail, across the northeast, our $E_h^{100}$ amplitude is highest at site VAQ58 in Virginia at 25.44 V/km; for the geomagnetic latitude (year 2000, approximately centered on the duration of our geomagnetic time series) and the physiographic region of this site, this is more than an order of magnitude higher than the 100-year benchmark amplitude (2.25 V/km) developed by NERC (2014) using one-dimensional Earth models. At site MEE62 in Maine, $E_h^{100}$ is 21.75 V/km (compared to just 3.18 V/km for the NERC benchmark); at site CTI60 in Connecticut our estimate is 19.39 V/km (while for NERC, it is just 2.59 V/km); $E_h^{100}$ amplitude is lowest at site VAQ55 in Virginia at 0.05 V/km (while for NERC it is much higher at 0.66 V/km). All of this illustrates the importance of using realistic estimates of Earth surface impedance when estimating geoelectric hazards.

## 8. Geological Context

The northeast region's geological structure has, over hundreds of millions of years, been shaped by continental collisions and rifting events (e.g., Rast, 1989; Roy, 1987). In reference to the generalized geology map shown in Figure 7c, the Appalachians are an ancient and highly eroded mountain chain. The crystalline Appalachians—the Blue Ridge and Piedmont mountain ranges and the New England Highlands—are deep-seated formations of electrically resistive, igneous and metamorphic rock (e.g., Murphy & Egbert, 2017, Figure 2). To the northwest lie the sedimentary Appalachians, including the Appalachian Basin (AB) and the Valley Ridge Province, the latter consisting of elongated fold and thrust belts of electrically conductive sedimentary rock. Farther to the northwest, the Appalachian Plateau and, to the southeast, the Atlantic Coastal Plain, consist of thick layers of electrically conducting sediment that has eroded from the mountains. The prevailing "strike" line is defined by the projection of geological features (faults, rock beds, intrusive formations, accretion boundaries, coastlines, etc.) onto the horizontal plane (e.g., Pollard & Fletcher, 2005, p. 54). For the Northeast region, the strike is southwest-to-northeast. Correspondingly, "dip" is defined as the downward inclination of rock bedding in directions orthogonal to the strike, and across the northeast, the dip tends to be down to the southeast or down to the northwest.

In comparing Figures 7a and 7b with 7c (Reed & Bush, 2007), we observe that the highest-amplitude geoelectric fields occur beneath the crystalline Appalachians and tend to be polarized in directions orthogonal to the general strike of the Appalachians. This suggests an important role in areas of high geoelectric hazard for what magnetotelluricists call the transverse-magnetic mode of induction (e.g., Berdichevsky & Dmitriev, 2008; Chave & Weidelt, 2012; Simpson & Bahr, 2005), whereby horizontal geoelectric fields (oriented parallel to a lateral conductivity gradient, or orthogonal to its strike) result from both the time-varying geomagnetic field (corresponding to Faraday induction) and the quasi-static buildup of electric charge (under dipping rock formations) and along lateral conductivity gradients (giving Coulomb fields). The transverse-magnetic mode of induction might explain some of the high geoelectric hazards beneath the Valley and Ridge Province that lies at the eastern edge of the Appalachian Basin, where conductive sedimentary rocks are juxtaposed against resistive structures of the crystalline Appalachians. Correspondingly, the transverse-electric mode of induction, whereby horizontal geoelectric fields (oriented orthogonal to a conductivity gradient, or parallel to its strike) only result from the time-varying geomagnetic field, apparently plays a less important role in high-hazard areas of the northeast. This result is consistent with the interpretation of Ogawa et al., (1996, p. 1598) that electric current flow is channeled along the strike of the Appalachians, or, conversely, electric currents are resisted across the strike of the Appalachians. The lowest geoelectric hazards shown in Figure 7 correspond to sedimentary settings, which are generally relatively conductive.

## 9. Applications

The geomagnetically induced voltage on an individual power grid line can be estimated by line integration of the projection of the geoelectric field onto the path of the power grid line,

$$V = \int_G \mathbf{E}_h \cdot \mathrm{d}\mathbf{l} \tag{8}$$

where the integration path $G$ is taken between grounding points. From this equation, we understand that the amplitude of the voltage depends on both the amplitude of the geoelectric field and the direction of the (possibly highly polarized) geoelectric field over the path $G$. Power lines can have dimensions of hundreds of kilometers, and, therefore, geomagnetically induced voltages on power grid lines can, very easily, attain hundreds of (quasi-direct) volts (e.g., Lucas et al., 2018). Under Ohm's law, and assuming a typical line resistance of (say) 1 ohm, geomagnetically induced currents of hundreds of amps can be realized during an intense storm, more than sufficient to damage high-voltage transformers (e.g., Girgis & Vedante, 2002). We have found, however, that the highest-amplitude geoelectric fields across the Northeast United States tend to be polarized orthogonal to the prevailing geological strike of the Appalachians. Therefore, power lines crossing the Appalachians (trending southeast/northwest) are apparently more exposed to geoelectric hazards than are those oriented southwest-to-northeast. This new insight might allow utility companies to better anticipate the response of existing power grid systems across the northeast to future magnetic storms, and it might even be useful for developing strategies for what lines/transformers to turn on/off during a magnetic storm to mitigate deleterious effects. We imagine that these results might also be useful for planning future power grid installations of improved resilience.

## 10. Additional Developments

A statistical analysis, similar to that presented here, could, conceivably, be extended to encompass the continental United States. Given the planned coverage of the EarthScope magnetotelluric survey and the number of magnetic observatories monitoring the region, this would amount to ~20 fold increase in the amount of data needing to be analyzed. To accommodate this, a more efficient algorithm would need to be designed for searching through many long geoelectric field time series for $E_h^m$ amplitudes. And, this would, then, need to be followed by a critical examination of the validity of interpolating across the sparse spatial distribution of observatories, similar to that presented here, but for the 10 or so observatories that might be used for estimating induction. In contrast to the analysis methods used here, detailed analyses of the spatiotemporal variation of geoelectric fields realized over the course of individual storms are being pursued in at least two different ways. First, physically plausible basis functions are fitted to observatory data (e.g., Amm & Viljanen, 1999; Pulkkinen et al., 2003) to obtain improved interpolation between geomagnetic measurements. Second, physics-based models of the magnetospheric-ionospheric system are used to simulate ground-level geomagnetic variation (e.g., Pulkkinen et al., 2003; Rigler et al., 2014). Either way, storm time geomagnetic field variation can be convolved with estimates of Earth surface impedance, either directly, using the magnetotelluric tensors themselves (as done for this report), or using models of solid-Earth electrical conductivity structure (like those constructed for traditional solid-Earth investigations). All of this could conceivably be extended to real-time mapping of the geoelectric field (e.g., Love, Rigler, et al., 2018).

**Acknowledgments**
We thank C. A. Finn, J. McCarthy, E. J. Rigler, J. L. Slate, and two anonymous persons for reviewing a draft manuscript. We thank A. D. Chave for useful conversations. This work was supported by the USGS Geomagnetism Program; G. M. Lucas is supported by a USGS Mendenhall postdoctoral fellowship. The OTT and STJ magnetic observatory data are available from the NRCan Geomagnetism Program (www.geomag.nrcan.gc.ca; 1979–2016); the FRD data (U.S. Geological Survey, 1901) are available from the USGS Geomagnetism Program (www.usgs.gov, 1983–2016); some of the observatory data are available through INTERMAGNET (www.intermagnet.org; 1991–2016). The EarthScope impedance tensors are available from the Data Management Center of the Incorporated Research Institutions for Seismology (ds.iris.edu/ds/products/emtf) (Kelbert et al., 2011).

## References

Abraham, S. (2002). *National transmission grid study* (pp. 1–93). Washington, DC: Department of Energy.

Abt Associates (2017). *Social and economic impacts of space weather in the United States* (pp. 1–70). Boulder, CO: written under contract for NOAA National Weather Service.

Allen, J., Frank, L., Sauer, H., & Reiff, P. (1989). Effects of the March 1989 solar activity. *Eos Transactions American Geophysical Union*, *70*(46), 1486–1488. https://doi.org/10.1029/89EO00409

Amm, O., & Viljanen, A. (1999). Ionospheric disturbance magnetic field continuation from the ground to the ionosphere using spherical elementary current systems. *Earth Planets Space*, *51*(6), 431–440. https://doi.org/10.1186/BF03352247

Asaoka, Y., Kawachi, A., Matsubara, Y., & Sasaki, M. (2003). The log-normal distributions of coronal mass ejection-related solar flares and the flare/CME model of gamma-ray bursts. In T. Kajita, Y. Asaoka, A. Kawachi, Y. Matsubara, & M. Sasaki (Eds.), *Proceedings of the 28th International Cosmic Ray Conference, July 31-August 7, 2003* (pp. 2729–2732), International Union of Pure and Applied Physics. Tokyo, Japan: Universal Academy Press.

Baker, D. N., Balstad, R., Bodeau. J. M., Cameron, E., Fennell. J. E., Fisher, G. M., et al. (2008). *Severe space weather events—Understanding societal and economic impacts* (pp. 1–144). Washington, DC: The National Academy Press. https://doi.org/10.17226/12507

Barnes, P. R., Rizy, D. T., McConnell, B. W., Tesche, F. M., & Taylor, E. R. Jr. (1991). *Electric utility industry experience with geomagnetic disturbances* (Vol. ORNL-6665, pp. 1–78). Oak Ridge, TN: Oak Ridge National Laboratory

Barnes, P. R., & Van Dyke, J. W. (1990). Economic consequences of geomagnetic storms (a summary). *IEEE Power Engineering Review*, *10*(11), 3–4. https://doi.org/10.1109/39.60450

Bedrosian, P. A., & Love, J. J. (2015). Mapping geoelectric fields during magnetic storms: Synthetic analysis of empirical United States impedances. *Geophysical Research Letters*, *42*, 10,160–10,170. https://doi.org/10.1002/2015GL066636

Béland, J., & Small, K. (2005). Space weather effects on power transmission systems: The Cases of Hydro-Québec and Transpower New Zealand Ltd. In I. A. Daglis (Ed.), *Effects of Space Weather on Technology Infrastructure* (pp. 287–299). Dordrecht, The Netherlands: Springer.

Berdichevsky, M. N., & Dmitriev, V. I. (2008). *Models and methods of magnetotellurics* (pp. 1–563). Berlin, Germany: Springer-Verlag.

Blum, C., Love, J. J., Pedrie, K., Bedrosian, P. A., & Rigler, E. J. (2015). A one-dimensional model of solid-earth electrical resistivity beneath Florida. *USGS Open-File Rep*, *98-782*, 1–16. https://doi.org/10.3133/ofr20151185

Bolduc, L. (2002). GIC observations and studies in the Hydro-Québec power system. *Journal of Atmospheric and Solar-Terrestrial Physics*, *64*(16), 1793–1802. https://doi.org/10.1016/S1364-6826(02)00128-1

Bonner, L. R., & Schultz, A. (2017). Rapid prediction of electric fields associated with geomagnetically induced currents in the presence of three-dimensional ground structure: Projection of remote magnetic observatory data through magnetotelluric impedance tensors. *Space Weather*, *15*, 204–227. https://doi.org/10.1002/2016SW001535

Burlaga, L. G., & Lazarus, A. J. (2000). Lognormal distributions and spectra of solar wind plasma fluctuations: Wind 1995–1998. *Journal of Geophysical Research*, *105*(A2), 2357–2364. https://doi.org/10.1029/1999JA900442

Chave, A. D. (2012). Estimation of the magnetotelluric response function. In A. D. Chave & A. G. Jones (Eds.), *The magnetotelluric method* (pp. 165–218). Cambridge, UK: Cambridge University Press.

Chave, A. D. (2017). *Computational statistics in the Earth sciences* (pp. 1–451). Cambridge, UK: Cambridge University Press.

Chave, A. D., & Jones, A. G. (Eds.) (2012). *The magnetotelluric method* (pp. 1–552). Cambridge, UK: Cambridge University Press.

Chave, A. D., & Weidelt, P. (2012). The theoretical basis for electromagnetic induction. In A. D. Chave, & A. G. Jones (Eds.), *The magnetotelluric method* (pp. 19–49). Cambridge, UK: Cambridge University Press.

Connecticut Geological Survey (2013). *Generalized bedrock map of connecticut*. Hartford, CT: Department of Energy and Environmental Protection.

Efron, B., & Tibshirani, R. J. (1993). *An introduction to the bootstrap*. Dordrecht, The Netherlands: Springer Science+Business Media.

Egbert, G. D. (1992). Noncausality of the discrete-time magnetotelluric impulse response. *Geophysics*, *57*(10), 1354–1358. https://doi.org/10.1190/1.1443204

Egbert, G. D. (2007a). Robust electromagnetic transfer functions estimates. In D. Gubbins, & E. Herrero-Bervera (Eds.), *Encyclopedia of geomagnetism and paleomagnetism* (pp. 866–870). Dordrecht, The Netherlands: Springer.

Egbert, G. D. (2007b). EM modeling, inverse. In D. Gubbins, & E. Herrero-Bervera (Eds.), *Encyclopedia of geomagnetism and paleomagnetism* (pp. 219–223). Dordrecht, The Netherlands: Springer.

Evans, R. L. (2012). Earth's electromagnetic environment: 3A. Conductivity of Earth materials. In A. D. Chave, & A. G. Jones (Eds.), *The magnetotelluric method* (pp. 50–95). Cambridge, UK: Cambridge University Press.

Federal Energy Regulatory Commission (2013). Reliability standards for geomagnetic disturbances. *Federal Register, Rules and Regulations*, *78*(100), 30,747–30,762.

Ferguson, I. J. (2012). Instrumentation and field procedures. In A. D. Chave, & A. G. Jones (Eds.), *The Magnetotelluric Method* (pp. 421–479). Cambridge, UK: Cambridge University Press.

Ferguson, I. J., & Odwar, H. D. (1997). Review of conductivity soundings in Canada, Appendix 3. In D. H. Boteler (Ed.), *Geomagnetically induced currents: Geomagnetic hazard assessment, phase II, 357 T 848A* (Vol. 3, pp. 1–121). Geol. Surv. Canada and Canadian Electr. Assoc.

Fernberg, P. (2012). *One-dimensional Earth resistivity models for selected areas of continental United States & Alaska* (pp. 1–190). Palo Alto, CA: EPRI Technical Update 1026430.

Florida, R., Gulden, T., & Mellander, C. (2008). The rise of the mega-region. *Cambridge Journal of Regions Economy and Society*, *1*(3), 459–476. https://doi.org/10.1093/cjres/rsn018

Gannon, J. L., Trichtchenko, L., & Fernberg, P. (2012). United States regional GIC hazard assessment, *Abstract fall meeting*. San Francisco, Calif.: AGU. SM21D-08.

Girgis, R., & Vedante, K. (2002). Effects of GIC on power transformers and power systems. *IEEE Transactions on Power Delivery*, *17*(4), 1002–1008. https://doi.org/10.1109/TPWRD.2002.803710

Gottman, J. (1961). *Megalopolis: The urbanized northeastern seaboard of the United States* (pp. 1–810). New York, NY: The Twentieth Century Fund.

Kappenman, J. (2012). A perfect storm of planetary proportions. *IEEE Spectrum*, *49*, 26–31. https://doi.org/10.1109/MSPEC.2012.6139230

Kelbert, A., Balch, C. C., Pulkkinen, A., Egbert, G. D., Love, J. J., Rigler, E. J., & Fujii, I. (2017). Methodology for time-domain estimation of storm time geoelectric fields using the 3-D magnetotelluric response tensors. *Space Weather*, *15*, 874–894. https://doi.org/10.1002/2017SW001594

Kelbert, A., Egbert, G. D., & Schultz, A. (2011). IRIS DMC data services products: EMTF, the magnetotelluric transfer functions. https://doi.org/10.17611/DP/EMTF

Laske, G., & Masters, G. (1997). A global digital map of sediment thickness. *Eos Transactions American Geophysical Union*, *78*, F483.

Lloyd's of London (2013). *Emerging risk report: Solar storm risk to the North American electric grid* (pp. 1–22). London, UK.

Loiselle, M. (2002). *Simplified bedrock geologic map of Maine* (Vol. SBGMM, 24). Open-File Map: Maine Geological Survey.

Love, J. J., & Finn, C. A. (2011). The USGS geomagnetism program and its role in space weather monitoring. *Space Weather*, *9*, S07001. https://doi.org/10.1029/2011SW000684

Love, J. J., Lucas, G. M., Kelbert, A., & Bedrosian, P. A. (2018a). Geoelectric hazard maps for the Mid-Atlantic United States: 100-year extreme values and the 1989 magnetic storm. *Geophysical Research Letters*, *45*, 5–15. https://doi.org/10.1002/2017GL076042

Love, J. J., Lucas, G. M., Kelbert, A., & Bedrosian, P. A. (2018b). Geoelectric hazard maps for the Pacific Northwest. *Space Weather*, *16*, 1114–1127. https://doi.org/10.1029/2018SW001844

Love, J. J., Rigler, E. J., Kelbert, A., Finn, C. A., Bedrosian, P. A., & Balch, C. C. (2018). On the feasibility of real-time mapping of hazardous geoelectric fields across North America. (USGS Open-File Report, 2018-1043), 1–16. https://doi.org/10.3133/ofr20181043

Love, J. J., Rigler, E. J., Pulkkinen, A., & Riley, P. (2015). On the lognormality of historical magnetic storm intensity statistics: Implications for extreme-event probabilities. *Geophysical Research Letters*, *42*, 6544–6553. https://doi.org/10.1002/2015GL064842

Lucas, G. M., Love, J. J., & Kelbert, A. (2018). Calculation of voltages in electric power transmission lines during historic geomagnetic storms: An investigation using realistic Earth impedances. *Space Weather*, *16*, 185–195. https://doi.org/10.1002/2017SW001779

Marti, L., Yiu, C., Rezaei-Zare, A., & Boteler, D. (2014). Simulation of geomagnetically induced currents with piecewise layered-Earth models. *IEEE Transactions on Power Delivery*, *29*(4), 1186–1193. https://doi.org/10.1109/TPWRD.2014.2317851

McKay, A. J., & Whaler, K. A. (2006). The electric field in northern England and southern Scotland: Implications for geomagnetically induced currents. *Geophysical Journal International*, *167*(2), 613–625. https://doi.org/10.1111/j.1365-246X.2006.03128.x

Molinski, T. S. (2002). Why utilities respect geomagnetically induced currents. *Journal of Atmospheric and Solar-Terrestrial Physics*, *64*(16), 1765–1778. https://doi.org/10.1016/S1364-6826(02)00126-8

Murphy, B. S., & Egbert, G. D. (2017). Electrical conductivity structure of Southeastern North America: Implications for lithospheric architecture and Appalachian topographic rejuvenation. *Earth and Planetary Science Letters*, *462*, 66–75. https://doi.org/10.1016/j.epsl.2017.01.009

National Science and Technology Council (2015). *National space weather action plan* (pp. 1–38). Washington, DC: Executive Office.

Newell, P. T., Sotirelis, T., Liou, K., Meng, C. I., & Rich, F. J. (2007). A nearly universal solar wind-magnetosphere coupling function inferred from 10 magnetospheric state variables. *Journal of Geophysical Research*, *112*, A01206. https://doi.org/10.1029/2006JA012015

Newitt, L. R., & Coles, R. (2007). Observatories in Canada. In D. Gubbins, & E. Herrero-Bervera (Eds.), *Encyclopedia of geomagnetism and paleomagnetism* (pp. 726–727). Dordrecht, The Netherlands: Springer.

Ngwira, C. M., Pulkkinen, A. A., Bernabeu, E., Eichner, J., Viljanen, A., & Crowley, G. (2015). Characteristics of extreme geoelectric fields and their possible causes: Localized peak enhancements. *Geophysical Research Letters*, *42*, 6916–6921. https://doi.org/10.1002/2015GL065061

Nikitina, L., Trichtchenko, L., & Boteler, D. (2016). Assessment of extreme values in geomagnetic and geoelectric field variations for Canada. *Space Weather*, *14*, 481–494. https://doi.org/10.1002/2016SW001386

North American Electric Reliability Corporation (1990). March 13, 1989 geomagnetic disturbance, *1989 System Disturbances* (pp. 36–60). Princeton, NJ.

North American Electric Reliability Corporation (2014). *Benchmark geomagnetic disturbance event description* (pp. 1–26). Atlanta, GA.

Nye, D. E. (2010). *When the lights went out: A history of blackouts in America* (pp. 1–304). Cambridge, MA: MIT Press.

Ogawa, Y., Jones, A. G., Unsworth, M. J., Booker, J. R., Lu, X., Craven, J., et al. (1996). Deep electrical conductivity structures of the Appalachian Orogen in the southeastern U.S. *Geophysical Research Letters*, *23*(13), 1597–1600. https://doi.org/10.1029/95GL03601

Piccinelli, R., & Krausmann, E. (2014). *Space weather and power grids—A vulnerability assessment* (pp. 1–53). Luxembourg: European Union.

Pirjola, R. (2002). Review on the calculation of surface electric and magnetic fields and of geomagnetically induced currents in ground-based technological systems. *Surveys in Geophysics*, *23*(1), 71–90. https://doi.org/10.1023/A:10148160

Pollard, D. D., & Fletcher, R. C. (2005). *Fundamentals of structural geology* (pp. 1–503). Cambridge, UK: Cambridge University Press.

Prölss, G. W. (2004). *Physics of the Earth's space environment* (pp. 1–513). Berlin, Germany: Springer-Verlag.

Pulkkinen, A., Amm, O., Viljanen, A., & BEAR working group (2003). Ionospheric equivalent current distributions determined with the method of spherical elementary current systems. *Journal of Geophysical Research*, *108*(A2), 117–129. https://doi.org/10.1029/2001JA005085

Pulkkinen, A., Bernabeu, E., Eichner, J., Beggan, C., & Thomson, A. W. P. (2012). Generation of 100-year geomagnetically induced current scenarios. *Space Weather*, *10*, S04003. https://doi.org/10.1029/2011SW000750

Pulkkinen, A., Bernabeu, E., Eichner, J., Viljanen, A., & Ngwira, C. (2015). Regional-scale high-latitude extreme geoelectric fields pertaining to geomagnetically induced currents. *Earth Planets Space*, *67*, 93. https://doi.org/10.1186/s40623-015-0255-6

Rast, N. (1989). The evolution of the Appalachian chain. In A. W. Bally, & A. R. Palmer (Eds.), *The geology of North America: An overview* (Vol. A, pp. 323–348). Boulder, CO: Geological Soc. Am.https://doi.org/10.1130/DNAG-GNA-A.323

Reed, J. C., & Bush, C. A. (2007). About the geologic map in the National Atlas of the United States of America. *USGS Circular*, *1300*, 1–52.

Rigler, E. J., Pulkkinen, A. A., Balch, C. C., & Wiltberger, M. J. (2014). Dynamic geomagnetic hazard maps in space weather operations, *Abstract Fall Meeting*. San Francisco, Calif.: AGU. SM31A-4178.

Riley, P., & Love, J. J. (2017). Extreme geomagnetic storms: Probabilistic forecasts and their uncertainties. *Space Weather*, *15*, 53–64. https://doi.org/10.1002/2016SW001470

Rodi, W. L., & Mackie, R. L. (2012). The inverse problem. In A. D. Chave & A. G. Jones (Eds.), *The magnetotelluric method* (pp. 347–420). Cambridge, UK: Cambridge University Press.

Rossi, C. E. (1990). Failure of electrical power equipment due to solar magnetic disturbances (Information Notice No. 90-42). Washington, DC.

Roy, D. C. (Ed.) (1987). *Northeastern section of the geological society of America* (Centennial Field Guide (Book 5), pp. 1–517). Boulder, CO: Geological Society of America.

Samuelsson, O. (2013). *Geomagnetic disturbances and their impact on power systems*. Sweden: Ind. Elec. Eng. Auto., Lund University.

Schultz, A. (2010). A continental scale magnetotelluric observatory and data discovery resource. *Data Science Journal*, *8*, IGY6–IGY20.

Schultz, A., Egbert, G. D., Kelbert, A., Peery, T., Clote, V., Fry, B., Erofeeva, S., & staff of the National Geoelectromagnetic Facility and their contractors (2006). USArray TA magnetotelluric transfer functions. https://doi.org/10.17611/DP/EMTF/USARRAY/TA

Simpson, F., & Bahr, K. (2005). *Practical magnetotellurics* (pp. 1–254). Cambridge, UK: Cambridge University Press.

Solanki, S. K., Schüssler, M., & Fligge, M. (2002). Secular variation of the Sun's magnetic flux. *Astronomy & Astrophysics*, *383*(2), 706–712. https://doi.org/10.1051/0004-6361:20011790

Steinskog, D. J., Thøstheim, D. B., & Kvamstø (2007). A cautionary note on the use of the Kolmogorov-Smirnov test for normality. *Monthly Weather Review*, *135*(3), 1151–1157. https://doi.org/10.1175/MWR3326.1

Stratton, J. A. (1941). *Electromagnetic theory* (pp. 1–615). New York, NY: McGraw-Hill Book Company.

Trichtchenko, L., Fernberg, P. A., & Danskin, D. W. (2016). Geoelectric field modelling for Canadian space weather services. *Canadian Geological Survey, Open File*, *8115*, 1–140. https://doi.org/10.4095/299116

U.S. Geological Survey (1901). Geomagnetism program definitive data. INTERMAGNET. Other/seismic network. https://doi.org/10.7914/SN/NT

Unsworth, M. (2007). Magnetotellurics. In D. Gubbins, & E. Herrero-Bervera (Eds.), *Encyclopedia of geomagnetism and paleomagnetism* (pp. 670–673). Dordrecht, The Netherlands: Springer.

Vassiliadis, D., Klimas, A. J., Valdivia, J. A., & Baker, D. N. (1999). The Dst geomagnetic response as a function of storm phase and amplitude and the solar wind electric field. *Journal of Geophysical Research*, *104*, 24,957–24,976. https://doi.org/10.1029/1999JA900185

Veselovsky, I. S., Dmitriev, A. V., & Suvorova, A. V. (2010). Algebra and statistics of the solar wind. *Cosmic Research*, *48*, 113–128.

Vicino, T. J., Hanlon, B., & Short, J. R. (2007). Megalopolis 50 years on: The transformation of a city region. *International Journal of Urban and Regional Research*, *31*, 344–367. https://doi.org/10.1111/j.1468-2427.2007.00728.x

Virginia Division of Mineral Resources (1993). *Geologic map of Virginia*. Charlottesville, VA.

Wait, J. R. (1982). *Geo-electromagnetism* (pp. 1–268). New York, NY: Academic Press.
Watermann, J., Rasmussen, O., Stauning, P., & Gleisner, H. (2006). Temporal versus spatial geomagnetic variations along the west coast of Greenland. *Advances in Space Research*, *37*(6), 1163–1168. https://doi.org/10.1016/j.asr.2005.08.019
Wei, L. H., Homeier, N., & Gannon, J. L. (2013). Surface electric fields for North America during historical geomagnetic storms. *Space Weather*, *11*, 451–462. https://doi.org/10.1002/swe.20073
Weidelt, P., & Chave, A. D. (2012). The magnetotelluric response function. In A. D. Chave & A. G. Jones (Eds.), *The Magnetotelluric Method* (pp. 122–164). Cambridge, UK: Cambridge University Press.
Weigel, R. S. (2017). A comparison of methods for estimating the geoelectric field. *Space Weather*, *15*, 430–440. https://doi.org/10.1002/2016SW001504
Williams, M. L., Fischer, K. M., Freymueller, J. T., Tikoff, B., & Tréhu, A. M. (2010). *Unlocking the secrets of the North American Continent: An EarthScope science plan for 2010–2020* (pp. 1–78). EarthScope.
Yoshino, T. (2011). Electrical properties of rocks. In H. K. Gupta (Ed.), *Encyclopedia of solid Earth geophysics* (pp. 270–276). Dordrecht, The Netherlands: Springer-Verlag.
Yurchyshyn, V., Yashiro, S., Abramenko, V., Wang, H., & Gopalswamy, N. (2005). Statistical distributions of speeds of coronal mass ejections. *The Astrophysical Journal*, *619*(1), 599–603. https://doi.org/10.1086/426129